



Fractional Fourier-Radial Transform for Digital Image Recognition

Luis Felipe López-Ávila¹ · Josué Álvarez-Borrego¹ · Selene Solorza-Calderón²

Received: 20 August 2019 / Revised: 2 January 2020 / Accepted: 5 May 2020
© Springer Science+Business Media, LLC, part of Springer Nature 2020

Abstract

This paper presents a new system for pattern recognition in digital images, called Fractional Fourier-Radial Transform, invariant to translation, scale and rotation (TSR invariant) taking advantage of the well-known properties of some integral transform as Fourier Transform, Mellin Transform and the Radial Hilbert Transform. The main contribution of this work is the use of the Fractional Fourier Transform to avoid, or reduce the overlap between results due to the optimal order selection for each reference image, assuming $\alpha = \beta$ for computing optimization, which helps to get a higher difference between the reference images spectrum. This system was tested using different species of phytoplankton obtaining a level of confidence of at least 92.68% invariant to position, size, and rotation, supporting scale variations of $\pm 20\%$. The mean of the highest confidence values for the scale variation correlations is 98.47%, for rotation variation correlations is 100%, and for the rotation and scale variation correlations is 98.15%. The testing dataset images are selected due to their morphology complexity; they have a real pattern to be recognized instead of using a test-book data set.

Keywords Fourier transform · Fractional Fourier transform · Mellin transform · Pattern recognition · TSR invariant

1 Introduction

Since the introduction of the classical matched filter by Van der Lugt in 1964 [1], the pattern recognition has become a fundamental part of the industrial and health sectors, which makes it one of the main fields in image processing research.

The objective is to identify patterns in digital images, for this, different techniques have been developed depending on the characteristics of the pictures as those acquired by Guerrero-Moreno and Álvarez-Borrego in 2009 [2] where they used a nonlinear composite filter, the results produced by Lerma-Aragón and Álvarez-Borrego in 2009 [3] where they designed a methodology to get Translation, Scale and Rotation (TRS) invariant vectorial signatures; and many others [4–11], but there are still some complications, such as the TRS invariant recognition of objects using a single target

image (not composite filters) and the increase of the scale range with high effectiveness.

Using the module of the Fourier Transform, which is invariant to translation [12], then performing the Mellin transform to generate the invariance to scale [13] and finally applying the fractional Fourier-radial transform, proposed in this work to create the rotation invariance, four signatures TSR invariant are generated. The fractional Fourier-radial transform proposed in this work is based on the works developed about the Hilbert transform, such as its optical implementation developed by Lohmann et al. [14], the spatial filtering to obtain the isotropic Hilbert transform developed by Ojeda-Castañeda and Jara [15] and particularly the Hilbert radial transform developed by Alcaráz [16] where an invariant rotation methodology for image recognition is developed.

The main contribution of this Fractional Fourier-Radial Transform is to avoid, or reduce, the overlap between results due to the optimal order selection for each reference image. This methodology has been designed to create a more significant difference between different images because each image has its optimal order of fractional Fourier-radial transform. This work takes advantage of these integral transforms to design a new technique (explained below) to improve the results about time and handling for a user, the use of only one reference image is necessary.

One of the most used methods for comparing data is the correlation [17–22], due to its easy implementation in the

✉ Josué Álvarez-Borrego
josue@cicese.mx

¹ CICESE, Applied Physics Division, Optics Department, Carretera Ensenada-Tijuana No. 3918, Fraccionamiento Zona Playitas, C. P. 22860 Ensenada, Mexico

² UABC, Science Faculty, Carretera Ensenada-Tijuana Km. 103, C. P. 22860 Ensenada, Mexico

plane of frequencies. In this work, a classical correlation, normalized by the Pearson coefficient [23], is used to compare the signatures of the images.

The size of the images in the dataset is 320×320 . But when generating translation, scale and rotation invariance of a model, four-vectors of 26 lengths are calculated with the vital information of the original image, and they are compared, these are called signatures. In this way, 26 elements are used instead of 102,400, which means an advantage of computing time during the performance of correlation. This is also a great advantage over storage because once the 26 elements have been obtained, it is not necessary to keep the 102,400 and it will only store 26 elements per image.

The rest of the paper is organized as follows. In Section 2, the definition of Mellin Transform, Fractional Fourier Transform, and Fractional Fourier-Radial Transform is presented. The methodology is written in Section 3. Computer simulations and results are presented in Section 4, and in Section 5 conclusion are given. This work improves the results on the user’s time of implementation. So, identifying objects in digital images using a single reference image regardless of the position, scale, or rotation and use the fractional Fourier transform to increase the degree of freedom and manipulation of the methodology.

2 Mathematical Basis

2.1 Mellin Transform

The two dimensional Mellin transform [24, 25] is defined by

$$F_M(s, t) = M\{f(x, y)\} = \int_0^\infty \int_0^\infty f(x, y)x^{s-1}y^{t-1} dx dy, \tag{1}$$

where s and t are the variables of the coordinate system in the Mellin space.

When calculating the Mellin transform of a scaled function by a factor λ , $F_M^\lambda(s, t) = M\{f(\lambda x, \lambda y)\}$, we can conclude (2)

$$|F_M(s, t)| = |F_M^\lambda(s, t)|. \tag{2}$$

In this way, the module of the Mellin Transform is invariant to scale. If we calculate the module of the Fourier Transform of an image, to take advantage of its translation invariance, and then calculate the module of the Mellin Transform from the previous result, we obtain an image invariant to translation and scale.

2.2 Fractional Fourier Transform

The fractional Fourier transform is an integral transform [26–32], which is interpreted as a generalized form of the conventional Fourier transform, where the physical

meaning of this fractional Fourier transform is the electric field distribution that describes the different diffraction patterns along the propagation of the wavefront of an electromagnetic wave.

The expression for the two dimensional fractional Fourier transform is

$$F_{\alpha, \beta}(u, v) = \mathcal{F}^{\alpha, \beta}\{f(x, y)\} = \int_{-\infty}^\infty \int_{-\infty}^\infty f(x, y)K_{\alpha, \beta}(x, y, u, v) dx dy, \tag{3}$$

where the kernel is defined by

$$K_{\alpha, \beta}(x, y, u, v) = \sqrt{1 - i \cot \phi_\alpha} \exp[i\pi(x^2 + u^2) \cot \phi_\alpha - i2\pi u x \csc \phi_\alpha] \times \sqrt{1 - i \cot \phi_\beta} \exp[i\pi(y^2 + v^2) \cot \phi_\beta - i2\pi v y \csc \phi_\beta], \tag{4}$$

where ϕ_α and ϕ_β are the rotation angles in the plane space-spatial frequency for each coordinate and are given by

$$\phi_\alpha = \alpha \frac{\pi}{2}, \quad \phi_\beta = \beta \frac{\pi}{2} \tag{5}$$

where α and β are the orders of the fractional Fourier transform in x and y directions respectively.

2.3 Fractional Fourier-Radial Transform

The radial Hilbert transform [16, 33–35] is defined by

$$\mathcal{H}_R\{f(x, y)\} = e^{ip\theta} F(u, v), \tag{6}$$

where p is the order of the radial Hilbert transform, $\theta = \arccos(\frac{u}{r})$, with $r = \sqrt{u^2 + v^2}$ for $(u, v) \neq (0, 0)$ and $F(u, v)$ is the Fourier transform of the function $f(x, y)$.

Since $e^{ip\theta}$ takes complex values it can be expressed by

$$e^{ip\theta} = H(u, v) = \text{Re}[H(u, v)] + i \text{Im}[H(u, v)], \tag{7}$$

where $\text{Re}[H] = \sin(p\theta)$, $\text{Im}[H] = \cos(p\theta)$ and using the next conditions

$$\text{Re}[H(u, v)] = \begin{cases} 1 & \text{for } \sin(p\theta) > 0, \\ 0 & \text{for } \sin(p\theta) \leq 0 \end{cases}, \tag{8}$$

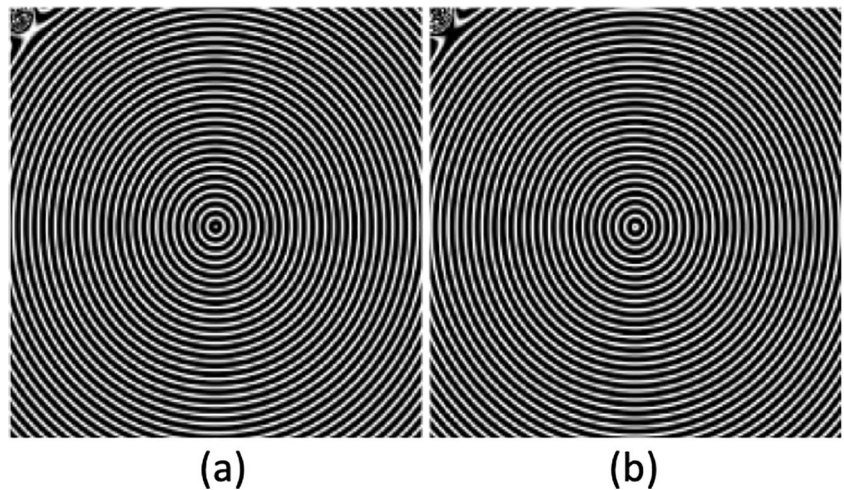
$$\text{Im}[H(u, v)] = \begin{cases} 1 & \text{for } \cos(p\theta) > 0 \\ 0 & \text{for } \cos(p\theta) \leq 0 \end{cases}$$

it is possible to show the real and imaginary parts of function $H(u, v)$ (Fig. 1).

Filtering the frequencies of $\text{Re}[H]$ and $\text{Im}[H]$ using a binary disk D the masks $H_R = \text{Re}[H] \cdot D$ and $H_I = \text{Im}[H] \cdot D$ are generated. Figure 2 shows the binary disk D and the masks H_R and H_I .

Finally, two vectors can be obtained, where the number of elements of each signature is equal to the numbers of rings in each mask and the value of each

Figure 1 **a** Real part, $\text{Re}[H]$, of order $p = 1$. **b** Imaginary part, $\text{Im}[H]$, of order $p = 1$.



component is similar to the sum of the pixel values contained in each ring after the multiplication of the Fourier transform, $F(u, v)$, by each mask [16].

This work proposes a fractional Fourier-radial transform where the Fourier transform $F(u, v)$ in the Eq. (6) is replaced by the fractional Fourier transform $F_{\alpha, \beta}(u, v)$. Thus,

$$\mathcal{F}^{\alpha, \beta}\{H_{FR}[f(x, y)]\} = e^{ip\theta} F_{\alpha, \beta}(u, v), \tag{9}$$

in this way you have an additional parameter to manipulate, the order of the fractional Fourier transform (α and β). Each signature will have an optimal order for each image, not necessarily the same as the other image's signatures, and this very helpful for differentiating the results of the pictures that are different.

3 Methodology

3.1 Generation of Signatures S_{R-H_R} , S_{I-H_R} , S_{R-H_I} and S_{I-H_I}

Taking an image and calculating the module of the Fourier-Mellin transform, a new representative picture of the original

image is generated with the advantage that this new image is invariant to the position and scale of the original.

The Fractional Fourier Transform is calculated the fractional Fourier transform of order α, β ($\alpha = \beta$ in this work) and has its real and imaginary part. These are multiplied independently by each one of the masks shown in Fig. 2, and the pixel values of each resulting ring summed. In this way, we get rotation invariance, with the information given by the rings, regardless of the angle of rotation that the object presents. This invariance is because of modules of Fourier and Fourier-Mellin transform preserves the image rotation.

For producing signatures, every value summed in the ring is ordered according to a particular number of rings. Signatures are invariant to translation, scale, and rotation. Its maximum value will normalize these signatures. Figure 3 shows a diagram of the methodology explained above.

In this way, it is possible to generate equal signatures for the same object regardless of position, scale, and rotation. Figure 4 shows a representative diagram to obtain the same four signatures S_{R-H_R} , S_{I-H_R} , S_{R-H_I} and S_{I-H_I} for different images that contain the same object with different scale, position, and rotation.

Figure 2 **a** Binary disk. **b** H_R Mask. **c** H_I Mask.

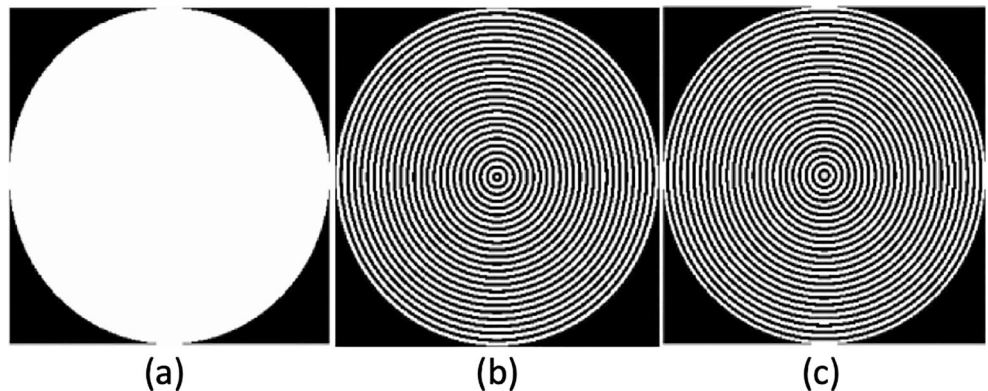
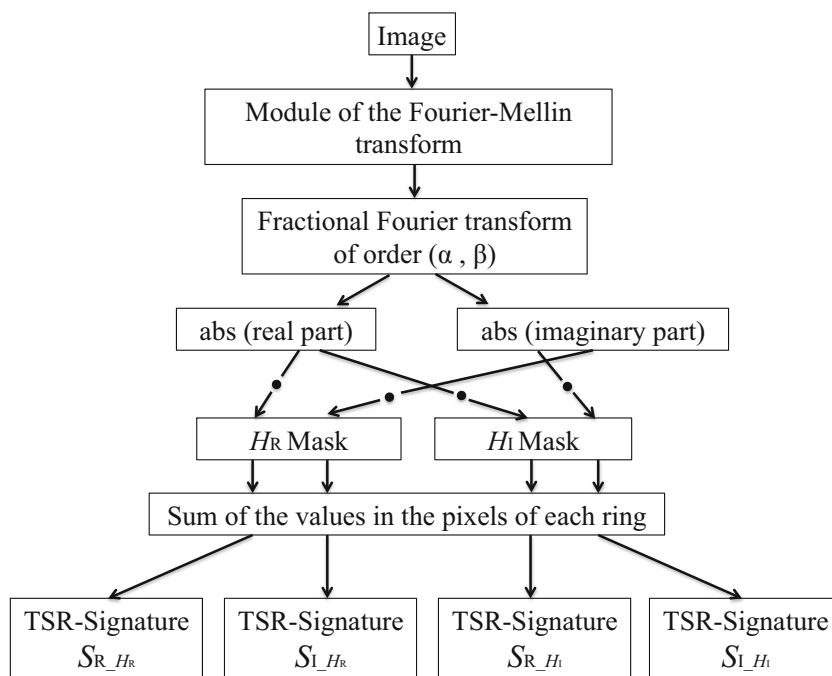


Figure 3 Methodology for the generation of the signatures S_{R-H_R} , S_{I-H_R} , S_{R-H_I} and S_{I-H_I} TSR invariants.



3.2 Signatures Correlations

Considering two images: the target and a problem image, it is natural to say: if the problem image is equal to the target, their signatures will be the same. While if the image to be recognized is different from the reference image; its signatures will not be equal. In a correlation between two signatures, it is expected that the maximum possible value is when the

signatures are identical and when the signatures are different smaller values are anticipated. Therefore, the correlation function is a proper metric to determine if the image to be identified is equal to the reference image or if they are different. This methodology is in the diagram presented in Fig. 5.

Before performing the correlation, the values of each signature are subtracted by the average of its signature. Then correlation values $C(S_{R-H_R}(RI), S_{R-H_R}(II))$,

Figure 4 Signatures S_{R-H_R} , S_{I-H_R} , S_{R-H_I} and S_{I-H_I} TSR invariants.

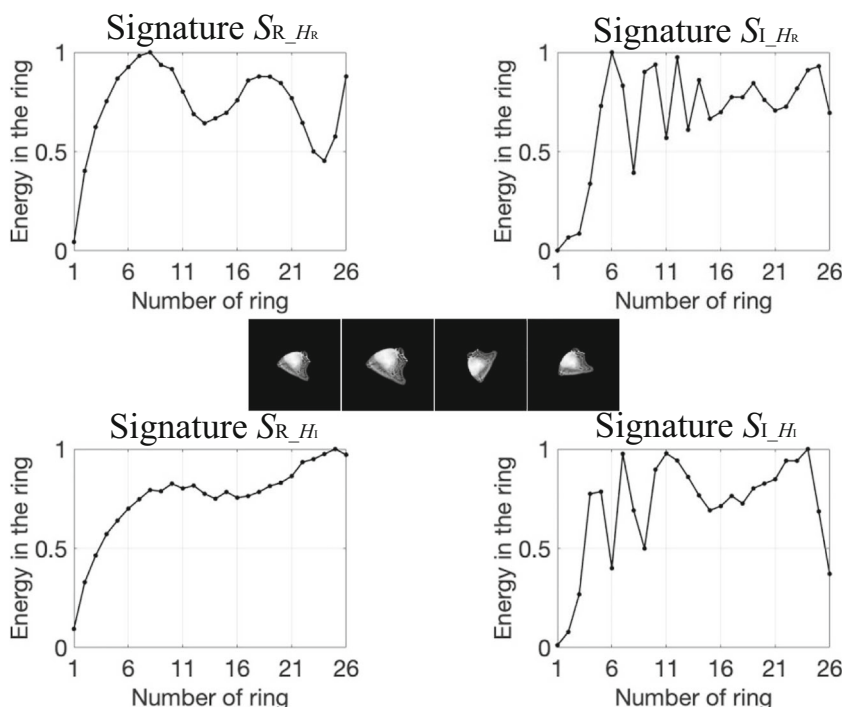


Figure 5 Signatures correlation methodology. RI: Reference image. II: Image to identify.

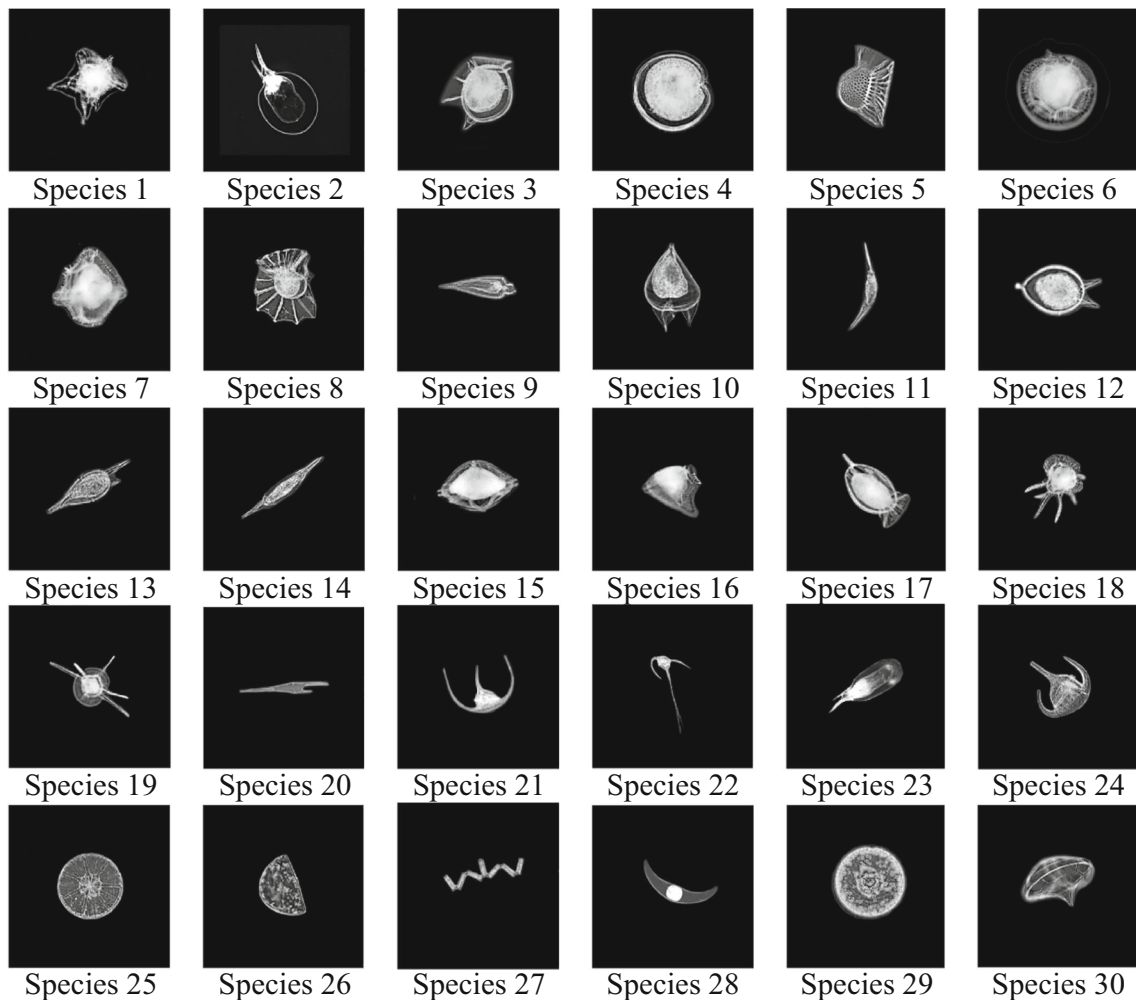
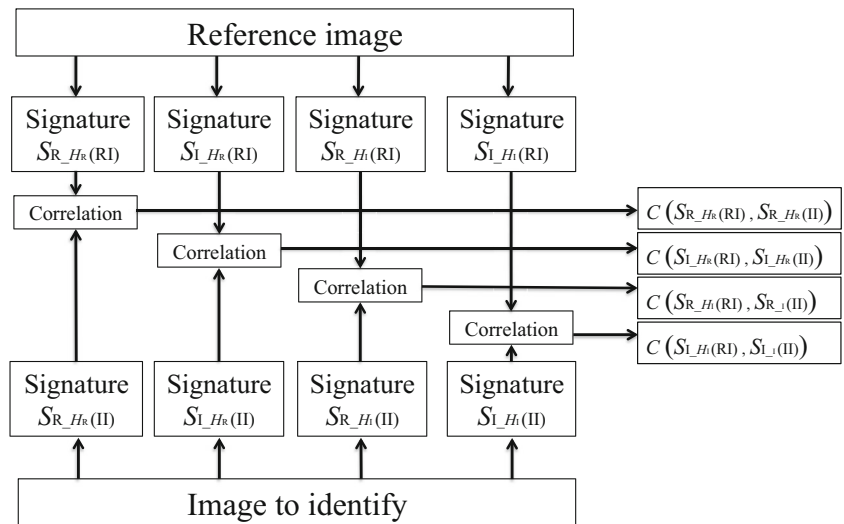


Figure 6 Phytoplankton species used in this analysis: 1 – *Acanthogonyaulax spinifera*, 2 – *Ceratium gravidum*, 3 *Dinophysis hastata*, 4 – *Diplosalopsis orbicularis*, 5 – *Histioneis*, 6 – *Lingolodinium polyedrum*, 7 – *Ornithocercu armata*, 8 – *Ornithocercus magnificus*, 9 – *Oxytoxum scolapax*, 10 – *Podolampas bipes 1*, 11 – *Podolampas spinifer 1*, 12 – *Podolampas bipes 2*, 13 – *Podolampas palmipes*, 14 – *Podolampa spinifer 2*, 15 – *Protoperidinium*, 16 –

Dinophysis rapa, 17 – *Dinophysis hastate*, 18 – *Ceratocorys horrida 1*, 19 – *Ceratocorys horrida 2*, 20 – *Ceratium furca*, 21 – *Ceratium lunula*, 22 – *Ceratium hexacatum*, 23 – *Ceratium praelongum*, 24 – *Ceratium breve*, 25 – *Asterolampira marylandica*, 26 – *Hemidiscus cuneiformis*, 27 – *Thalassionema nitzschioides*, 28 – *Pyrocystis*, 29 – *Hemidiscus*, and 30 – *Dinoflagellata*.

$C(S_{I_{H_R}}(RI), S_{I_{H_R}}(II))$, $C(S_{R_{H_I}}(RI), S_{R_{H_I}}(II))$ and $C(S_{I_{H_I}}(RI), S_{I_{H_I}}(II))$ are calculated using the Eqs. (10), (11), (12) and (13) respectively.

$$C(S_{R_{H_R}}(RI), S_{R_{H_R}}(II)) = \max \left[\frac{\text{cov}(S_{R_{H_R}}(RI), S_{R_{H_R}}(II))}{\text{std}(S_{R_{H_R}}(RI)) \times \text{std}(S_{R_{H_R}}(II))} \right] \tag{10}$$

$$C(S_{I_{H_R}}(RI), S_{I_{H_R}}(II)) = \max \left[\frac{\text{cov}(S_{I_{H_R}}(RI), S_{I_{H_R}}(II))}{\text{std}(S_{I_{H_R}}(RI)) \times \text{std}(S_{I_{H_R}}(II))} \right] \tag{11}$$

$$C(S_{R_{H_I}}(RI), S_{R_{H_I}}(II)) = \max \left[\frac{\text{cov}(S_{R_{H_I}}(RI), S_{R_{H_I}}(II))}{\text{std}(S_{R_{H_I}}(RI)) \times \text{std}(S_{R_{H_I}}(II))} \right] \tag{12}$$

$$C(S_{I_{H_I}}(RI), S_{I_{H_I}}(II)) = \max \left[\frac{\text{cov}(S_{I_{H_I}}(RI), S_{I_{H_I}}(II))}{\text{std}(S_{I_{H_I}}(RI)) \times \text{std}(S_{I_{H_I}}(II))} \right] \tag{13}$$

As you can see in Eqs. (10–13), the numerator is the covariance of the signatures and the denominator is the multiplication of the standard deviations of the signatures.

3.3 Optimal Order Selection for each Reference Image

The optimal order is that of the fractional Fourier transform that generates the highest autocorrelation value for each reference image. Autocorrelations will be made for the four signatures from the spatial plane ($\alpha = \beta = 0$) to the plane of frequencies ($\alpha = \beta = 1$) with increments of 0.01, to determine this value for each reference image. If we continue advancing after the plane of frequencies, we will be returning to the inverted spatial plane. An appraisal will be obtained for each autocorrelation. The order of the fractional Fourier transform with the highest correlation value will be the optimal order, so an optimal order corresponds to each signature of the reference image. This step is crucial in this methodology because each signature of each image will have its optimal order. Then the fractional Fourier-radial transform will be different for each signature of each image, which generates a more significant differentiation between the signatures of different pictures.

4 Computer Simulations

First, the next 30 images of different phytoplankton species were selected for the test of the algorithm (Fig. 6). These images were chosen due to the similarity and complexity between them to test the effectiveness of this methodology.

Then, the optimal order for the four signatures of each image was calculated, Table 1 shows those optimal orders. In Table 1, you can see that for some species, the optimal order is equal to one; that is, the fractional Fourier transform becomes the conventional Fourier transform of each image.

Each image is resized from 80% to 120% in 5% intervals; nine images are obtained for each image, which gives a total of 270 copies (Fig. 7 shows an example for species 1). Taking as a reference each of the pictures without scaling (100% scale) and making correlations in their optimal order using Eqs. (10–13), Table 2 is obtained.

Table 1 Optimal order for the fractional Fourier-radial transform for the four signatures.

Optimal order for the fractional Fourier-radial transform				
Image	Signatures			
	$S_{R_{H_R}}$	$S_{I_{H_R}}$	$S_{R_{H_I}}$	$S_{I_{H_I}}$
1	0.99	0.89	1.00	0.78
2	0.90	0.88	0.87	0.90
3	0.99	0.87	0.99	0.77
4	0.99	0.83	0.99	0.78
5	0.99	0.88	0.99	0.89
6	0.82	0.72	1.00	0.77
7	0.75	0.82	1.00	0.78
8	0.99	0.88	0.99	0.89
9	0.90	0.88	0.87	0.90
10	0.99	0.88	0.99	0.89
11	0.91	0.88	0.87	1.00
12	0.99	0.87	0.99	0.90
13	0.90	0.88	0.87	1.00
14	0.91	1.00	0.92	1.00
15	0.99	0.87	0.99	1.00
16	0.99	0.89	1.00	0.78
17	0.99	0.87	0.99	0.77
18	0.99	0.89	0.99	0.78
19	0.99	0.88	0.99	0.90
20	0.91	1.00	0.92	1.00
21	0.99	0.88	0.99	0.90
22	0.99	0.88	0.87	0.90
23	0.90	1.00	0.87	0.90
24	0.99	0.88	0.99	0.89
25	0.82	0.88	0.77	0.89
26	0.99	0.88	0.99	0.89
27	0.91	0.88	0.87	1.00
28	0.90	0.88	0.87	0.90
29	0.75	0.88	0.77	0.78
30	0.99	0.88	0.99	0.90

The black values mark the order of the conventional radial Hilbert transform

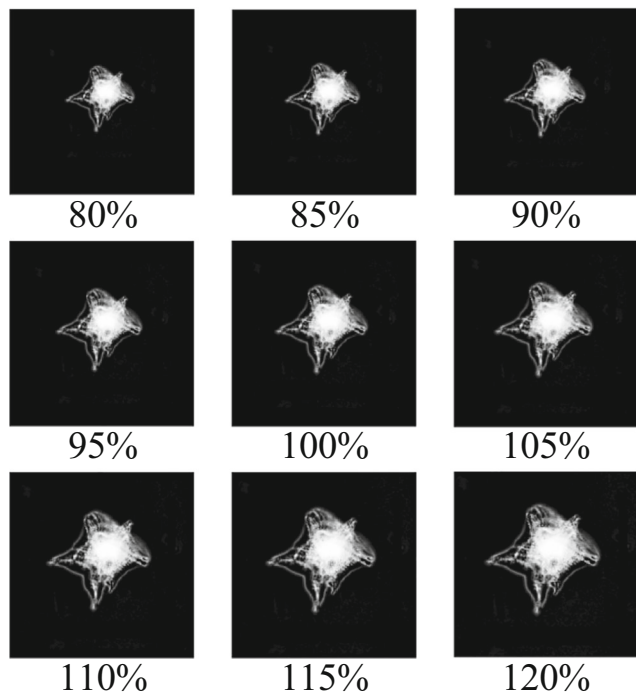


Figure 7 Phytoplankton species 1, scaled from 80% to 120% in 5% intervals.

You will notice that where the optimal order is equal to one, low confidence values were obtained compared with the rest of them and we will not consider these cases because the module of the Fourier-Mellin Transform moves us to the plane of frequencies and then when calculating the Fractional Fourier Transform in the order equal to one we move to the spatial plane, losing the information of the frequencies of the image. When the optimal order of a signature is similar to one, this signature will be useless, but we will still have the other signatures to identify the images we will only select the signature with the highest confidence level for each picture.

Figures 8, 9, 10, 11, 13, 14, 15, 16, 17, 18, 19 and 20 show an overlap of the box of the target species with some other boxes. Some values of correlation of species that we know are not the target were higher than the minimum amount of association of the target species. These values mean that our system mistakenly detects some other species. Analyzing the values that exceed the minimum correlation value of the target species versus the correlation values of all species, excluding the target species, the confidence level of this methodology can be calculated. This relationship is given by Eq. (14).

$$Confidence = 100\% \times \left(1 - \frac{\delta}{\tau}\right), \tag{14}$$

where δ is the number of correlations values that exceed the minimum correlation value of the target species (but are not from the target species) and τ number of correlation values of all species excluding the target species.

The boxplots shown in Figures 8, 9, 10, 11, 13, 14, 15, 16, 17, 18, 19 and 20 are centred in the mean and show the extreme values (empty boxes) and ± 2 standard errors (filled boxes). All the information is in the height of the boxes, the width is meaningless.

Each image was rotated in five degrees intervals, 72 images were obtained for each one, this gives a total of 2160 copies (Fig. 12 shows an example for species 1). Taking as a reference each of the images without rotating and making correlations in their optimal order, Table 3 is obtained. On Table 3, almost all the confidence values were 100%. We see shallow

Table 2 Correlations confidence for scale variation for the four signatures of each image.

Confidence of correlations for scale variation (%)				
Image	Signatures			
	S_{R_HR}	S_{I_HR}	S_{R_HI}	S_{I_HI}
1	95.40	96.93	96.55	97.32
2	95.40	95.40	95.40	95.40
3	92.34	98.08	92.72	99.23
4	82.38	97.70	85.44	99.23
5	91.57	92.72	92.34	93.49
6	97.70	98.47	96.55	100.00
7	97.70	96.55	95.79	96.55
8	90.04	94.64	90.04	95.02
9	96.17	96.55	96.55	97.32
10	96.93	100.00	96.93	100.00
11	100.00	100.00	100.00	17.24
12	94.25	91.19	94.25	93.87
13	100.00	100.00	100.00	3.83
14	100.00	6.51	99.23	7.66
15	97.70	96.93	97.70	27.59
16	94.64	96.93	96.93	96.55
17	97.70	98.08	97.70	98.08
18	98.85	100.00	98.85	100.00
19	100.00	100.00	100.00	100.00
20	100.00	4.98	99.62	3.07
21	100.00	100.00	100.00	100.00
22	98.47	100.00	100.00	99.62
23	96.55	3.07	96.93	97.32
24	95.40	98.85	95.79	99.23
25	97.32	95.79	96.17	95.40
26	96.55	100.00	96.55	100.00
27	100.00	100.00	100.00	69.73
28	98.47	95.79	98.47	97.32
29	100.00	98.85	100.00	100.00
30	97.32	100.00	98.08	100.00

The black values mark the highest confidence for each image

Figure 8 Results using the signatures S_{R-H_R} for correlations with scale variation using the species 1 as the target. (Above) all correlation boxes. (Below) zoom in the interest zone to show the overlap.

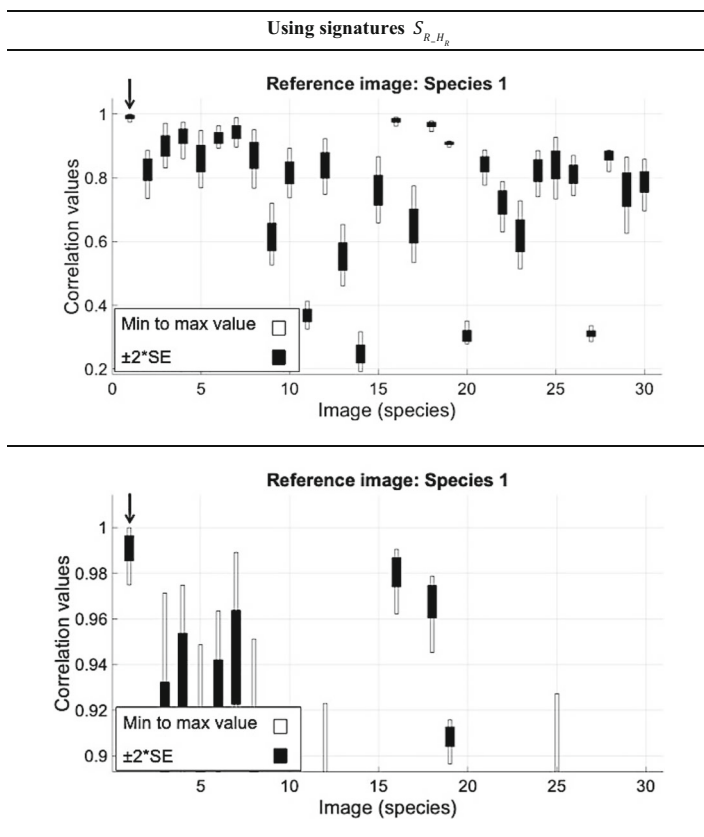


Figure 9 Results using the signatures S_{R-H_I} for correlations with scale variation using the species 1 as the target. (Above) all correlation boxes. (Below) zoom in the interest zone to show the overlap.

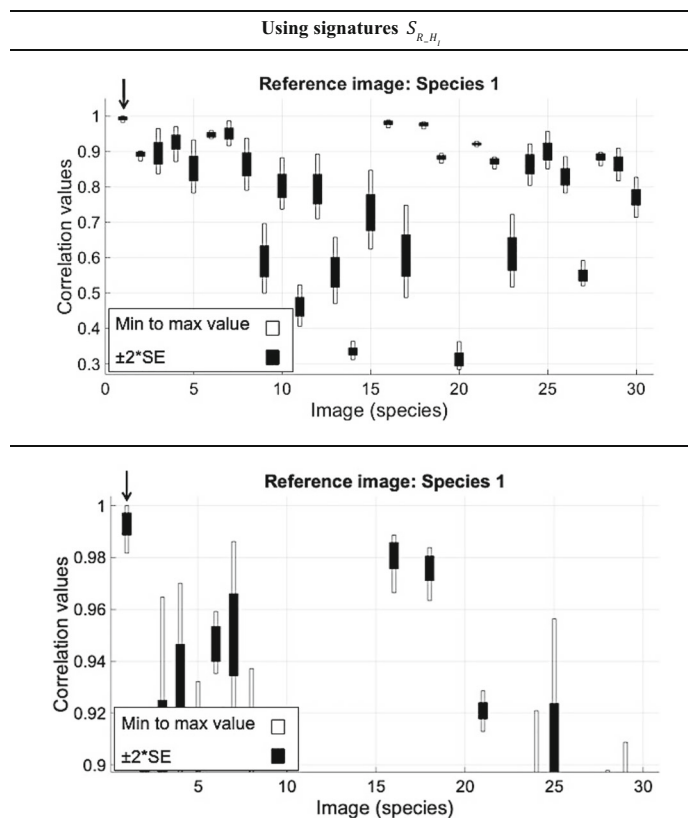


Figure 10 Results using the signatures S_{I-H_R} for correlations with scale variation using the species 1 as the target. (Above) all correlation boxes. (Below) zoom in the interest zone to show the overlap.

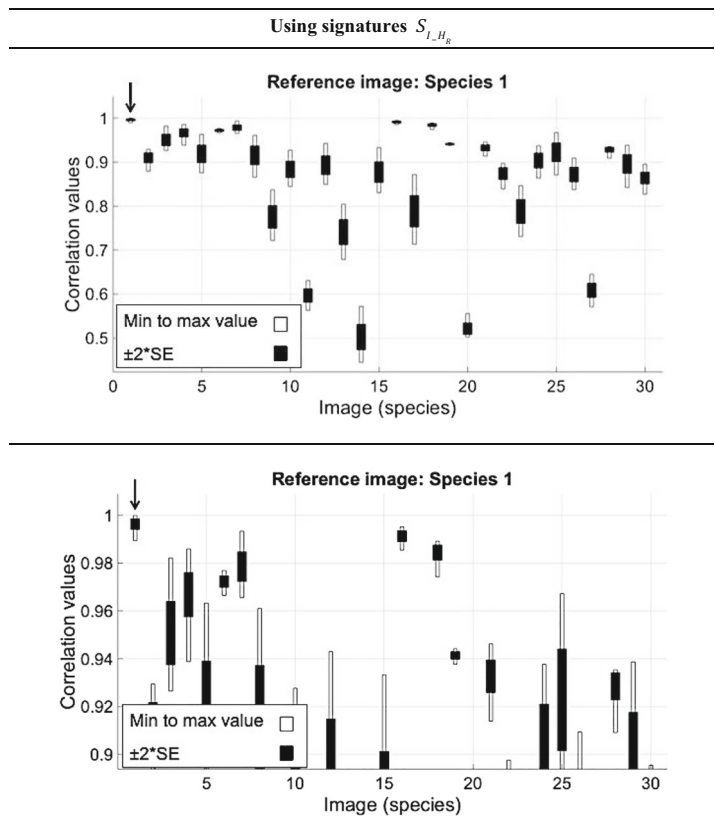
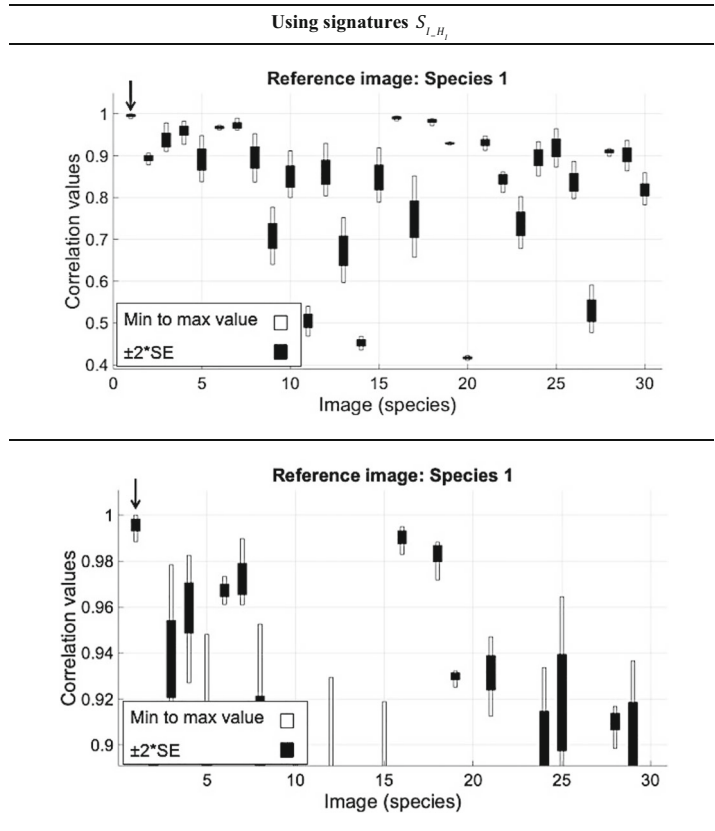


Figure 11 Results using the signatures S_{I-H_I} for correlations with scale variation using the species 1 as the target. (Above) all correlation boxes. (Below) zoom in the interest zone to show the overlap.



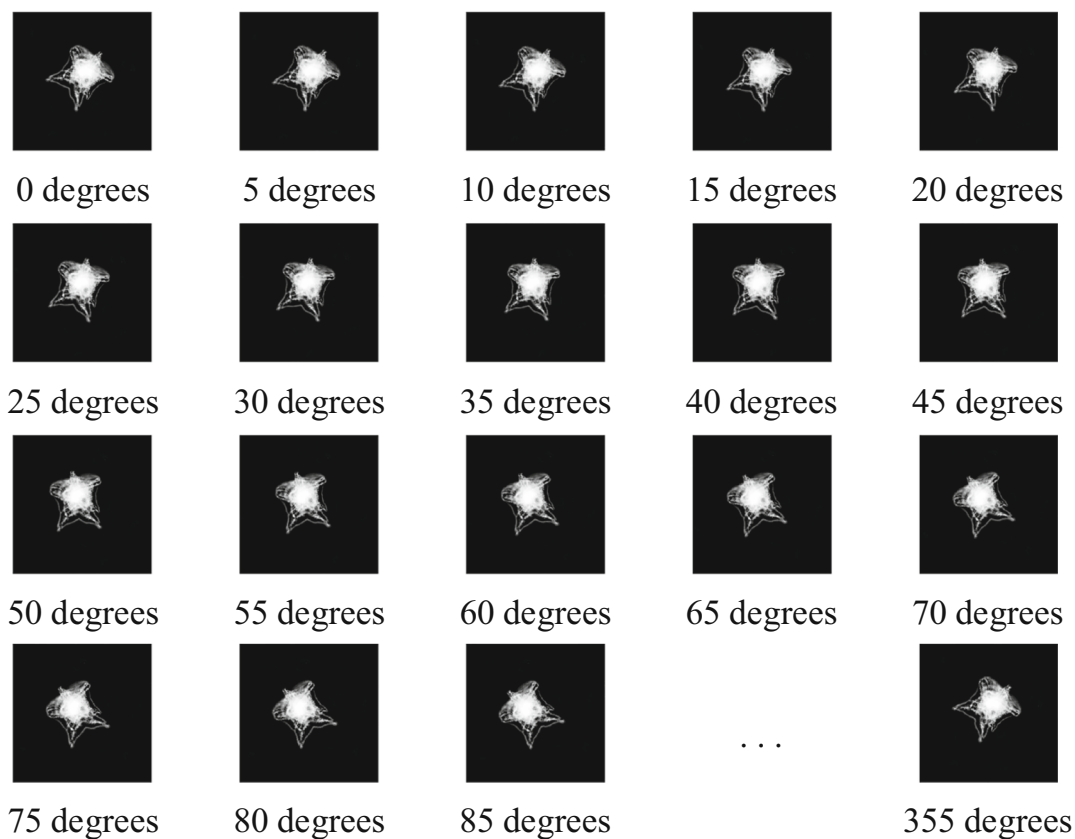


Figure 12 Phytoplankton species 1, rotated from 0 to 355 degrees in 5 degrees intervals.

Figure 13 Results using the signatures S_{R,H_R} for correlations with rotation variation using the species 1 as the target. (Above) all correlation boxes. (Below) zoom in the interest zone to show the overlap.

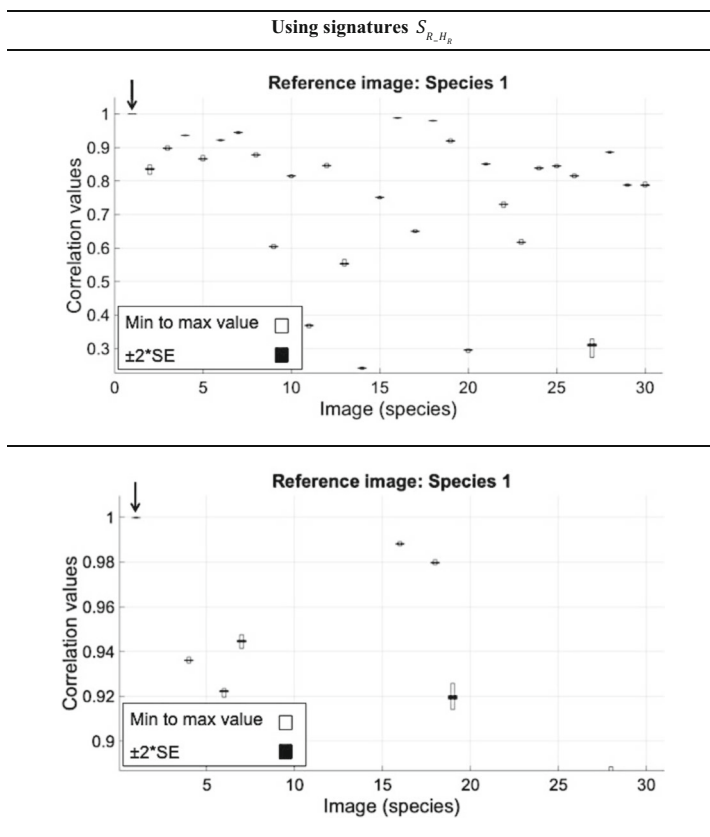


Figure 14 Results using the signatures $S_{R_H I}$ for correlations with rotation variation using the species 1 as the target. (Above) all correlation boxes. (Below) zoom in the interest zone to show the overlap.

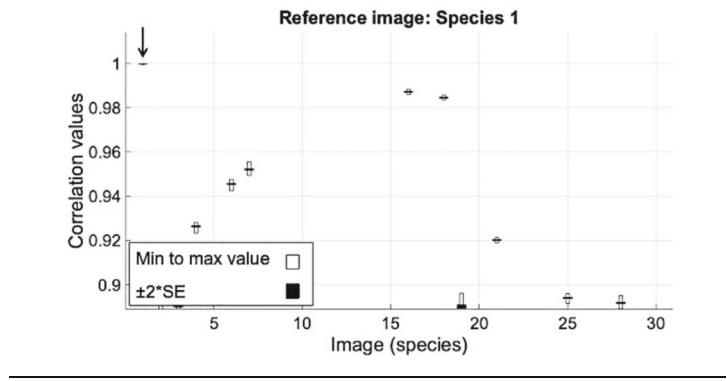
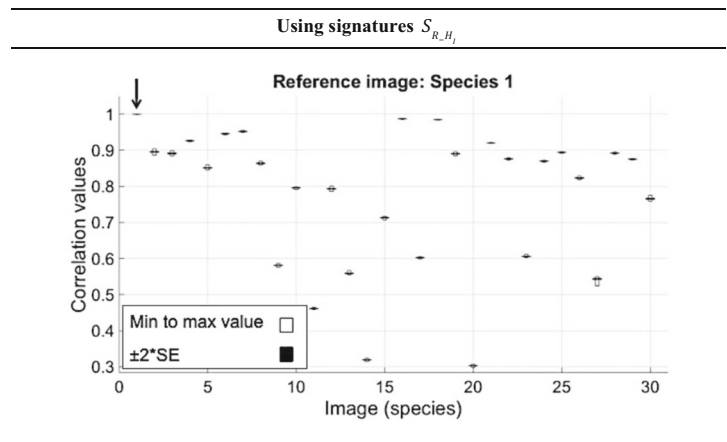


Figure 15 Results using the signatures $S_{I_H R}$ for correlations with rotation variation using the species 1 as the target. (Above) all correlation boxes. (Below) zoom in the interest zone to show the overlap.

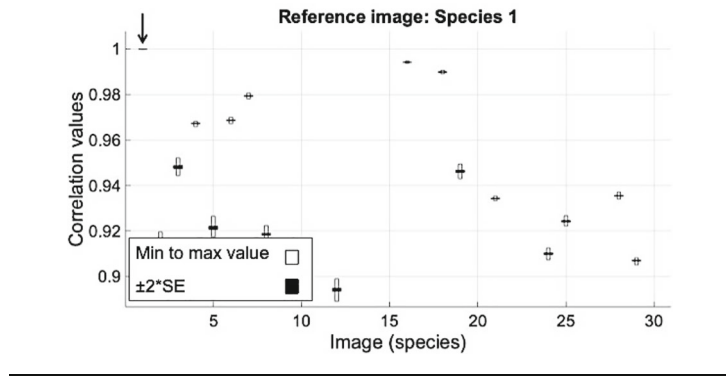
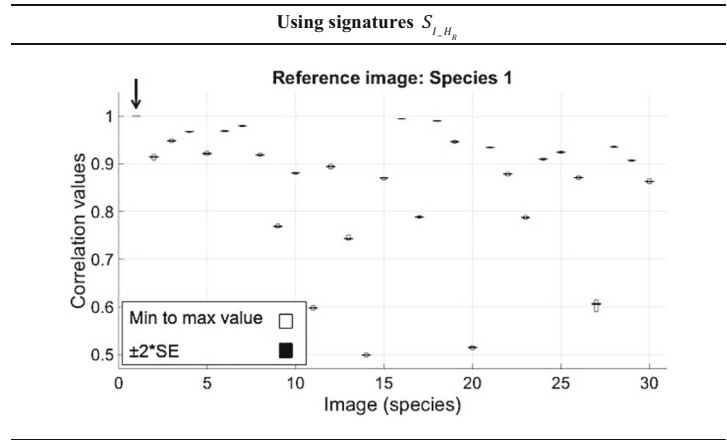


Figure 16 Results using the signatures S_{I,H_I} for correlations with rotation variation using the species 1 as the target. (Above) all correlation boxes. (Below) zoom in the interest zone to show the overlap.

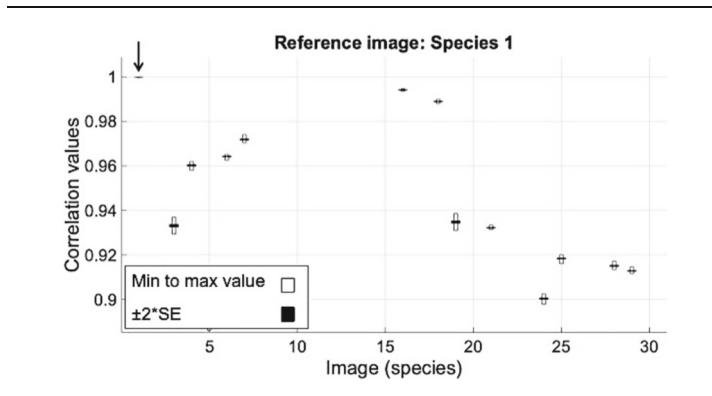
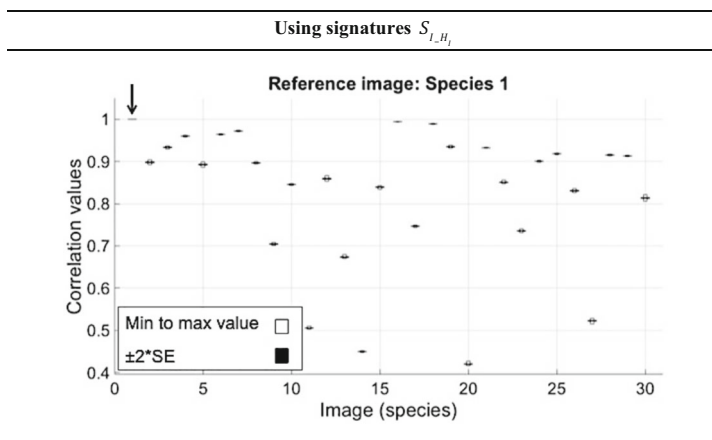


Figure 17 Results using the signatures S_{R,H_R} for correlations with rotation and scale variation using the species 1 as the target. (Above) all correlation boxes. (Below) zoom in the interest zone to show the overlap.

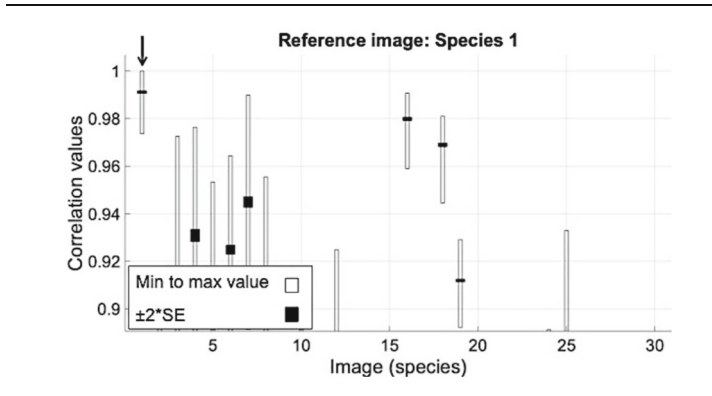
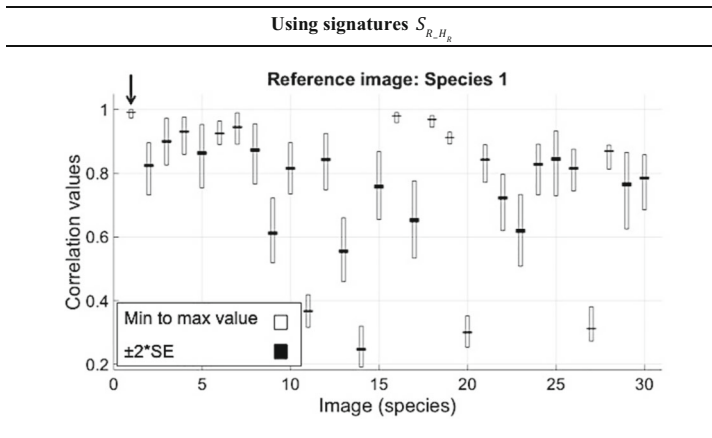


Figure 18 Results using the signatures S_{R,H_I} for correlations with rotation and scale variation using the species 1 as the target. (Above) all correlation boxes. (Below) zoom in the interest zone to show the overlap.

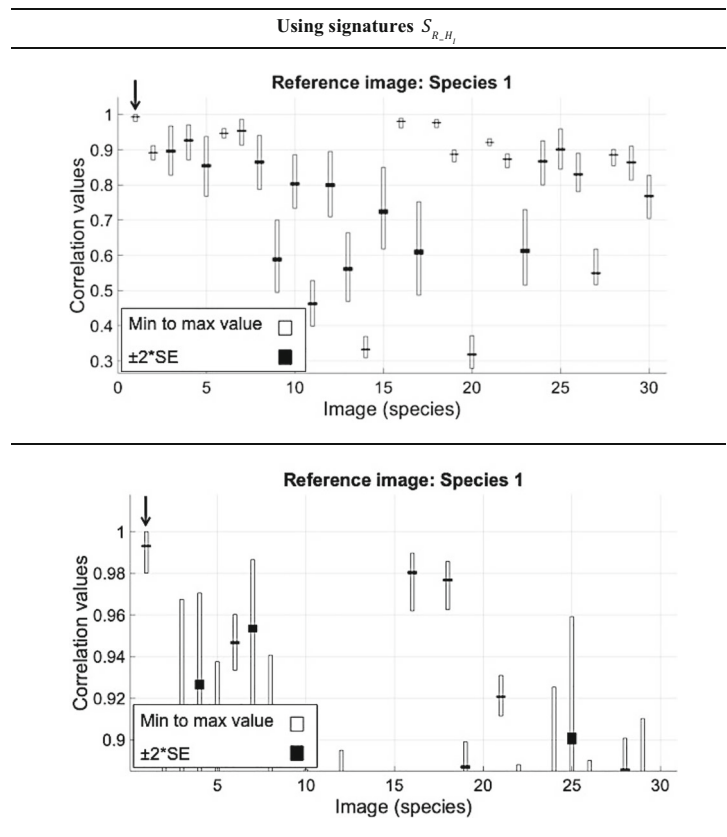


Figure 19 Results using the signatures S_{I,H_R} for correlations with rotation and scale variation using the species 1 as the target. (Above) all correlation boxes. (Below) zoom in the interest zone to show the overlap.

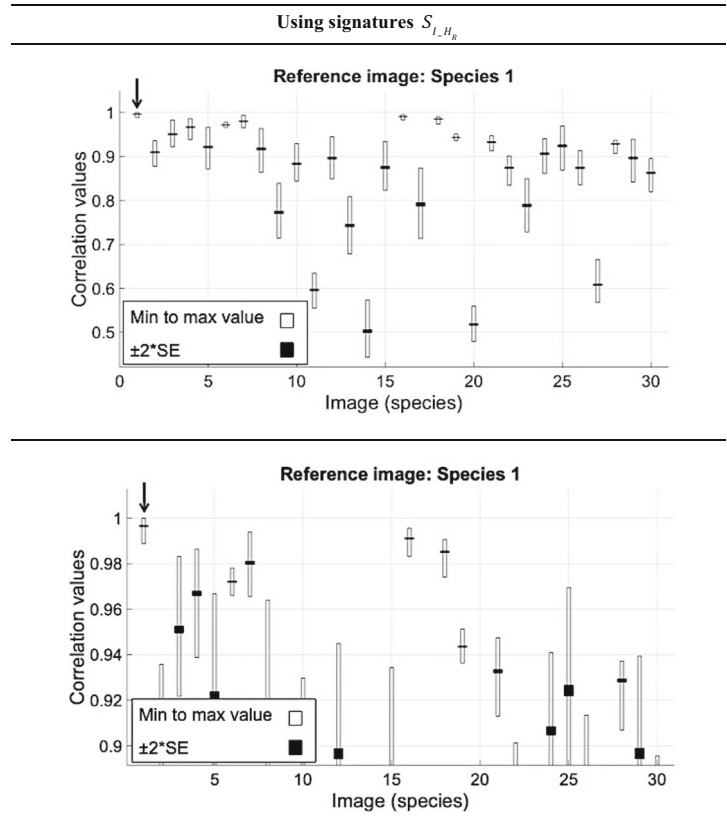
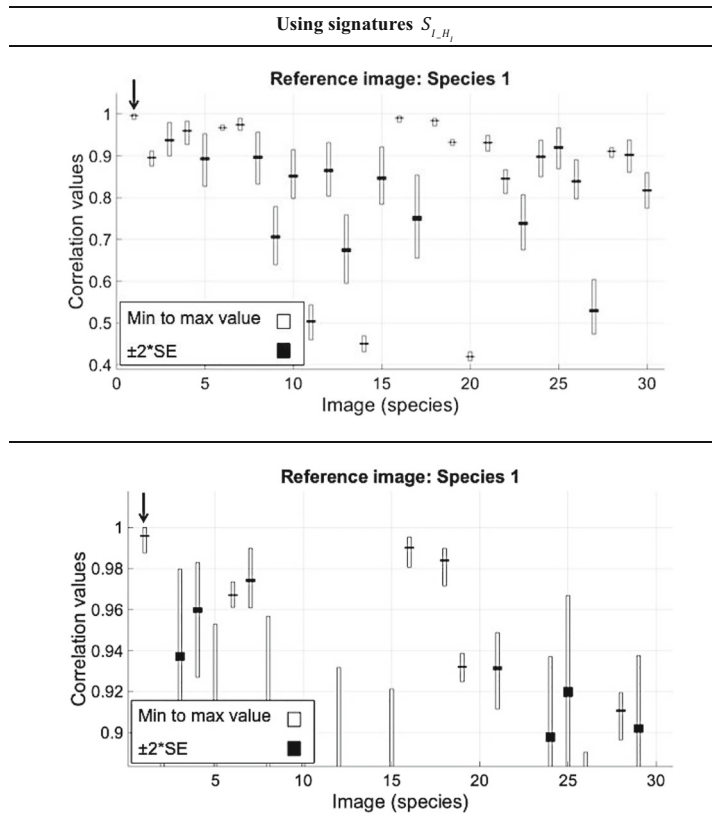


Figure 20 Results using the signatures S_{I,H_I} for correlations with rotation and scale variation using the species 1 as the target. (Above) all correlation boxes. (Below) zoom in the interest zone to show the overlap.



confidence values where the optimal orders are equal to one, but above, we explained why we would not consider these values. The Figs. 8, 9, 10 and 11 show the results using the four signatures for correlations with scale variation using the species one as the target and Figs. 13, 14, 15 and 16 show the results for rotation variation.

Each image was rotated in intervals of 5 degrees, 72 copies are obtained for each image, by scaling these 72 images from 80% to 120% in 5% intervals, a total of 19,440 images are generated. Taking as a reference each one of the images without rotating or scaling and making correlations in their optimal order, Table 4 is obtained, and again you can see shallow confidence values where the optimal order was equal to one, but we previously explained why we would not consider said values. The Figs. 17, 18, 19 and 20 show the results using the four signatures for correlations with rotation and scale variation using the species one as the target.

All calculations shown above were developed on a MacBook Pro computer with 2.5 GHz Intel Core i5 and 4 GB 1600 MHz DDR3 RAM.

These techniques for pattern recognition invariant to position, scale and rotation have been of great interest to the scientific community focused on image processing. In 1989 Reid developed an invariant technique to the position, scale and rotation for the recognition of patterns with an accuracy of

100% however in this work only the letters C and T were used with their different transformations [36]. Later in 1992 Spirkovska and Reid developed a new technique using neural networks reaching the 100% recognition accuracy for the test set for up to four occlusions of ~2% of the input field size and continue to show good performance for up to four occlusions of ~23% of the input field size each [37], but the neural networks must be training with hundreds of images.

In 1997 Levkovitz et al. extended the invariance of the Fang–Häusler transform to obtain a recognition process that can be successfully applied to binary images that simultaneously undergo extensive PRS (position, rotation and scale) changes. But their methodology doesn't work using gray scale images [38].

In more recent years, in 2012 Abdel-Kader et al. developed an invariant rotation methodology for the recognition of patterns in digital images reaching 99.5% recognition rate, however this methodology does not contemplate variations in position and scale. The methodology proposed in this work reaches 100% of the recognition rate using only rotation variations in the images [39].

Comparing these results with the ones obtained by Solorza and Álvarez-Borrego in 2015 [40] and by Garza-Flores and Álvarez-Borrego in 2018 [41] this methodology improves their results due to the fact that their results are only efficient to position and rotation variations, and this work is

suitable for position, rotation and scale variations. On the other hand, compared to the results obtained by Lerma-Aragón and Álvarez-Borrego [3], the results of the methodology shown in this work surpass theirs because they can identify the species using only one target with a high confidence level.

Solís-Ventura and Álvarez-Borrego [8] obtained results with a level of confidence of at least 95.4% using a methodology invariant to position, scale, and rotation, however they

Table 3 Correlations confidence for rotation variation for the four signatures of each image.

Confidence of correlations for rotation variation (%)				
Image	Signatures			
	S_{R_HR}	S_{I_HR}	S_{R_HI}	S_{I_HI}
1	100.00	100.00	100.00	100.00
2	100.00	100.00	100.00	100.00
3	100.00	100.00	100.00	100.00
4	100.00	100.00	100.00	100.00
5	100.00	100.00	100.00	100.00
6	100.00	100.00	100.00	100.00
7	100.00	100.00	100.00	100.00
8	100.00	100.00	100.00	100.00
9	100.00	100.00	100.00	100.00
10	100.00	100.00	100.00	100.00
11	100.00	100.00	100.00	0.24
12	100.00	100.00	100.00	100.00
13	100.00	100.00	100.00	2.87
14	100.00	1.77	100.00	2.30
15	100.00	100.00	100.00	3.21
16	100.00	100.00	100.00	100.00
17	100.00	100.00	100.00	100.00
18	100.00	100.00	100.00	100.00
19	100.00	100.00	100.00	100.00
20	100.00	3.16	100.00	3.54
21	100.00	100.00	100.00	100.00
22	100.00	100.00	100.00	100.00
23	100.00	2.30	100.00	100.00
24	100.00	100.00	100.00	100.00
25	100.00	100.00	100.00	100.00
26	100.00	100.00	100.00	100.00
27	100.00	100.00	100.00	4.69
28	100.00	100.00	100.00	100.00
29	100.00	100.00	100.00	100.00
30	100.00	100.00	100.00	100.00

The black values mark the lowest confidence for each image.

Table 4 Correlations confidence for rotation and scale variation for the four signatures of each image. The black values mark the highest confidence for each image.

Confidence of correlations for rotation and scale variation (%)				
Image	Signatures			
	S_{R_HR}	S_{I_HR}	S_{R_HI}	S_{I_HI}
1	94.70	95.96	96.19	96.15
2	95.52	95.04	95.40	95.00
3	91.74	96.40	92.06	98.79
4	82.80	97.00	85.22	99.47
5	90.70	92.68	91.09	92.53
6	97.45	97.74	95.47	100.00
7	97.38	96.64	95.58	96.64
8	87.25	90.51	87.02	92.69
9	96.25	96.64	96.30	97.04
10	96.23	100.00	95.89	99.13
11	100.00	100.00	100.00	0.24
12	93.81	90.39	93.70	93.66
13	99.49	100.00	99.81	0.30
14	99.87	0.04	98.93	0.07
15	97.62	96.57	97.62	0.10
16	94.25	95.73	96.64	96.40
17	97.70	98.08	97.70	98.08
18	98.90	100.00	98.93	100.00
19	100.00	100.00	100.00	100.00
20	99.78	0.17	98.23	0.25
21	98.62	98.66	98.98	99.02
22	98.47	99.60	100.00	98.87
23	96.40	0.01	96.17	96.93
24	94.64	98.81	94.66	98.68
25	96.62	94.74	95.74	95.00
26	96.21	99.62	96.17	99.56
27	100.00	100.00	100.00	1.67
28	98.30	95.55	98.28	96.83
29	100.00	98.83	100.00	100.00
30	97.42	99.53	96.70	98.87

used a range of scales of $\pm 10\%$ and an adaptive non-linear correlation, while the proposed method in this work uses a variety of scales of $\pm 20\%$ and a Pearson correlation, which is easier to implement, generating results a little lower than theirs, with a confidence level of 92.68% in the least.

The comparison of the results of this work with those obtained by Barajas-García et al. is complicated because the level of confidence obtained by them, which is at least 95%, is calculated using the Z-Fisher transform and in this work, it is not. However, the methodology proposed in this paper

accepts a scale range of $\pm 20\%$ and theirs only ± 10 , but their method is useful in the recognition of images even if they contain fragments of up to 49% of the area of the object.

5 Conclusions

It is possible to identify objects in digital images using the fractional Fourier-radial transform proposed in this work. All the photos reach at least 92.68% of confidence in all correlations. The mean of the highest confidence values for the scale variation correlations is 98.47%, for the rotation variation correlations it is 100%, and for the rotation and scale variation correlations its 98.15%. These results tell us about the high effectiveness of this new methodology.

Using the methodology presented, you obtain a confidence level of at least 92.68% invariant to position, scale, and rotation, supporting scale variations of $\pm 20\%$ and performing a straightforward correlation, and Pearson correlation.

In the case of obtaining a useless signature of an image, there are still three more signatures to use and select the best one, which reduces the probability of getting four unnecessary signatures of an image.

Acknowledgements Luis Felipe López-Ávila is a student in the Ph. D. program of Optics Department in CICESE (Centro de Investigación Científica y de Educación Superior de Ensenada) and supported by CONACyT's (Consejo Nacional de Ciencia y Tecnología) scholarship.

Compliance with Ethical Standards

Disclosures The authors reported no potential conflict of interest.

References

- Lugt, A. V. (1964). Signal detection by complex spatial filtering. *IEEE Transactions on Information Theory*, 10(2), 139–145.
- Guerrero-Moreno, R. E., & Álvarez-Borrego, J. (2009). Nonlinear composite filter performance. *Optical Engineering*, 48(6), 067201.
- Lerma-Aragón, J. R., & Álvarez-Borrego, J. (2009). Vectorial signatures for invariant recognition of position, rotation and scale pattern recognition. *Journal of Modern Optics*, 56(14), 1598–1606.
- Hoang, T.V. & Tabbone, S. (2010). A geometric invariant shape descriptor based on the Radon, Fourier, and Mellin transforms. In *Pattern Recognition (ICPR), IEEE 2010 20th International Conference on* pp. 2085–2088.
- Nacereddine, N. et al. (2010). Shape-based image retrieval using a new descriptor based on the radon and wavelet transforms. In *Pattern Recognition (ICPR), IEEE 2010 20th International Conference on* pp. 1997–2000.
- Solorza, S., & Álvarez-Borrego, J. (2010). Digital system of invariant correlation to position and rotation. *Optics Communication*, 283(19), 3613–3630.
- Álvarez-Borrego, J., Solorza, S., & Bueno-Ibarra, M. A. (2013). Invariant correlation to position and rotation using a binary mask applied to binary and gray images. *Optics Communication*, 294, 105–117.
- Solis-Ventura, A., Álvarez-Borrego, J., & Solorza, S. (2014). Adaptive nonlinear correlation with a binary mask invariant to rotation and scale. *Optics Communication*, 339, 185–193.
- Guerra-Rosas, E., & Álvarez-Borrego, J. (2015). Methodology for diagnosing of skin cancer on images of dermatologic spots by spectral analysis. *Biomedical Optics Express*, 6(10), 3876–3891.
- Barajas-García, C., Solorza-Calderón, S., & Álvarez-Borrego, J. (2016). Classification of fragments of objects by the Fourier masks pattern recognition system. *Optics Communication*, 367, 335–345.
- Guerra-Rosas, E., Álvarez-Borrego, J., & Angulo-Molina, A. (2017). Identification of phytoplankton species using Hermite transform. *Biomedical Optics Express*, 8(4), 2185–2194.
- Hsu, H.P. (1998). *Análisis de Fourier*. Addison Wesley Longman de México S. A. de C. V.
- Casasent, D., & Psaltis, D. (1976). Scale invariant optical transform. *Optical Engineering*, 15(3), 153258.
- Lohmann, A. W., Ojeda-Castañeda, J., & Díaz-Santana, L. (1996). Fractional Hilbert transform: Optical implementation for 1-D objects. *Optical Memory and Neural Networks*, 5(3), 131–135.
- Ojeda-Castañeda, J., & Jara, E. (1986). Isotropic Hilbert transform by anisotropic spatial filtering. *Applied Optics*, 25, 4035–4038.
- Alcaraz-Ubach, D.F. (2015) Applied mathematics bachelor thesis. Science Faculty, UABC.
- Gara, A. D. (1979). Real-time tracking of moving objects by optical correlation. *Applied Optics*, 18(2), 172–174.
- Bruck, H. A., McNeill, S. R., Sutton, M. A., & Peters III, W. H. (1989). Digital image correlation using Newton-Raphson method of partial differential correction. *Experimental Mechanics*, 29(3), 261–267.
- Davis, J. A., Waring, M. A., Bach, G. W., Lilly, R. A., & Cottrell, D. M. (1989). Compact optical correlator design. *Applied Optics*, 28(1), 10–11.
- Kumar, V., & Hassebrook, L. (1990). Performance measures for correlation filters. *Applied Optics*, 29(20), 2997–3006.
- Fimbres-Castro, C., et al. (2013). Nonlinear correlation by using invariant identity vectors signatures to identify plankton/Correlación no lineal utilizando firmas de vectores identidad para la identificación de plankton. *Gayana*, 77(2), 105–124.
- Take, W. A. (2015). Thirty-sixth Canadian geotechnical colloquium: Advances in visualization of geotechnical processes through digital image correlation. *Canadian Geotechnical Journal*, 52(9), 1199–1220.
- Benesty, J., et al. (2009). Pearson correlation coefficient. In noise reduction in speech processing (pp. 1–4). Berlin, Heidelberg: Springer.
- Casasent, D., & Psaltis, D. (1976). Scale invariant optical correlation using Mellin transforms. *Optics Communication*, 17(1), 59–63.
- Derrode, S., & Ghorbel, F. (2001). Robust and efficient Fourier–Mellin transform approximations for gray-level image reconstruction and complete invariant description. *Computer Vision and Image Understanding*, 83(1), 57–78.
- Namias, V. J. (1980). The fractional order Fourier transform and its application to quantum mechanics. *IMA Journal of Applied Mathematics*, 25(3), 241–265.
- Ozaktas, H. M., & Mendlovic, D. J. (1993). Fractional Fourier transforms and their optical implementation. II. *Journal of the Optical Society of America*, 10(12), 2522–2531.

28. Almeida, L. B. (1994). The fractional Fourier transform and time-frequency representations. *IEEE Transactions on Signal Processing*, 42(11), 3084–3091.
29. Pellat-Finet, P. (1994). Fresnel diffraction and the fractional-order Fourier transform. *Optics Letters*, 19(18), 1388–1390.
30. Mendlovic, D., Ozaktas, H. M., & Lohmann, A. W. (1995). Fractional correlation. *Applied Optics*, 34(2), 303–309.
31. Bitran, Y., Zalevsky, Z., Mendlovic, D., & Dorsch, R. G. (1996). Fractional correlation operation: Performance analysis. *Applied Optics*, 35(2), 297–303.
32. Ozaktas, H. M., Kutay, M. A., & Mendlovic, D. (1999). Introduction to the fractional Fourier transform and its applications. Chap 4. In P. W. Hawkes (Ed.), *Advances in imaging and electron physics* (pp. 239–291). New York: Academic.
33. Davis, J. A., McNamara, D. E., Cottrell, D. M., & Campos, J. (2000). Image processing with the radial Hilbert transform: Theory and experiments. *Optics Letters*, 25(2), 99–101.
34. Pei, S.C. & Ding, J.J. (2003) In *Acoustics, Speech, and Signal Processing, Proceedings. (ICASSP'03). 2003 IEEE International Conference on*, Vol. 3, pp. III-357.
35. King, F. W. (2009). *Hilbert transforms* (Vol. 1, pp. 1–858). Cambridge: Cambridge University Press.
36. Reid, M. B. (1989). Simultaneous position, scale, and rotation invariance pattern classification using third-order neural networks. *International Journal of Neural Networks*, 1, 154–159.
37. Spirkovska, L., & Reid, M. B. (1992). Robust position, scale, and rotation invariant object recognition using higher-order neural networks. *Pattern Recognition*, 25(9), 975–985.
38. Levkovitz, J., Oron, E., & Tur, M. (1997). Position-invariant, rotation-invariant, and scale-invariant process for binary image recognition. *Applied Optics*, 36(14), 3035–3042.
39. Abdel-Kader, R. F., Ramadan, R. M., Zaki, F. W., & El-Sayed, E. (2012). Rotation-invariant pattern recognition approach using extracted descriptive symmetrical patterns. *International Journal of Advanced Computer Science and Applications*, 3(5).
40. Solorza, S., & Álvarez-Borrego, J. (2015). Position and rotation-invariant pattern recognition system by binary rings masks. *Journal of Modern Optics*, 62(10), 851–864.
41. Garza-Flores, E., & Álvarez-Borrego, J. (2018). Pattern recognition using binary masks based on the fractional Fourier transform. *Journal of Modern Optics*, 65(14), 1634–1657.

Publisher's Note Springer Nature remains neutral with regard to jurisdictional claims in published maps and institutional affiliations.



Luis Felipe López-Ávila is a Ph. D. candidate at CICESE. He received his BS degree in physics from UABC and his MS degree in optics from CICESE in 2015 and 2017 respectively. His current research interests include image processing topics as object recognition, autonomous counting and classification methods. He is a member of AMO (Academia Mexicana de Óptica).



Josué Álvarez-Borrego is a researcher in the applied physics division at CICESE, leading the image processing group. He received his BS degree in oceanology from UABC, his MS and Ph. D. degrees in optics from CICESE in 1980, 1983 and 1993 respectively. He has published 85 scientific papers in ISI Journals, 93 papers in Conference Proceedings and he is author of 19 book chapters. He is currently president of the AMO (Academia Mexicana de Óptica).



Selene Solorza-Calderón is a researcher in the science faculty at UABC. She received her BS degree in applied mathematics from UABC, her MS and Ph. D. degrees in earth science from CICESE in 1997, 1999 and 2005 respectively. She has published 12 scientific papers in ISI Journals and she is author of 4 book chapters.